

Retina-Inspired Narrowband Perovskite Sensor Array for Panchromatic Imaging

Kai Wang (✉ kaiwang@psu.edu)

The Pennsylvania State University <https://orcid.org/0000-0003-2783-1288>

Yuchen Hou

The Pennsylvania State University

Junde Li

The Pennsylvania State University

Jungjin Yoon

The Pennsylvania State University

Abbey Knoepfel

The Pennsylvania State University

Dong Yang

Penn State <https://orcid.org/0000-0002-0518-019X>

Luyao Zheng

The Pennsylvania State University

Tao Ye

Pennsylvania State University <https://orcid.org/0000-0001-9381-8781>

Swaroop Ghosh

The Pennsylvania State University

Shashank Priya

Penn State University

Physical Sciences - Article

Keywords:

Posted Date: January 25th, 2022

DOI: <https://doi.org/10.21203/rs.3.rs-1104972/v1>

License: © ⓘ This work is licensed under a Creative Commons Attribution 4.0 International License.

[Read Full License](#)

Retina-Inspired Narrowband Perovskite Sensor Array for Panchromatic Imaging

Yuchen Hou,¹ Junde Li,³ Junjin Yoon,¹ Abbey Marie Knoepfel,¹ Dong Yang,^{1,2} Luyao Zheng,¹
Tao Ye,¹ Swaroop Ghosh,^{3*} Shashank Priya,^{1,2*} Kai Wang^{1,2*}

¹ Department of Materials Science and Engineering, Pennsylvania State University, University Park, PA 16802, USA

² Materials Research Institute, Pennsylvania State University, University Park, PA 16802, USA

³ School of Electrical Engineering and Computer Science, Pennsylvania State University, University Park, PA 16802 USA

Abstract

Retina, a thin layer of tissue, is the essential part of the human visual system that receives light, converts it to neural signal, and transmits it to the brain for visual recognition. The red, green, and blue (R/G/B) cone retina cells are natural narrowband photodetectors (PDs) sensitive to R/G/B lights. Connecting with these R/G/B cone cells, a multilayer neuro-network in the retina provides neuromorphic pre-processing for R/G/B signals before transmitting them to the brain. Inspired by this sophistication, in this study we develop the narrowband (NB) PD imaging sensor that combines the R/G/B perovskite NB sensor array (mimicking the R/G/B cone cells) with a neuromorphic algorithm (mimicking the intermediate network of the retinal system) for high-fidelity panchromatic imaging. Compared to commercial image sensors, we utilize perovskite *intrinsic* NB PD to exempt the complex optical filter array and thus avoiding issues such as color aliasing, limited quantum efficiency and demosaicing processing. Furthermore, we utilize an asymmetric device configuration to spontaneously collect photocurrent under zero external bias, enabling a power-free photodetection feature. Results of the novel perovskite image sensor along with the machine learning algorithm assisted image information correction, demonstrate a promising device for efficient and intelligent panchromatic imaging.

*Correspondence: SG: szg212@psu.edu; SP: sup103@psu.edu; KW: kaiwang@psu.edu

Introduction

Panchromatic image sensing of an object containing both shape and color information is advantageous than monochrome image sensing for a broad range of applications such as multispectral imaging/telecopy/clairvoyance in satellites¹, surveillance/microscopy smart-camera², and photography/film for aesthetics and entertainment³. In nature, the human retinal system is a highly sophisticated panchromatic sensing system with high-level of sensitivity (detectable of single photon⁴), resolution (576 megapixels⁵), and intelligence (capable of chromatic adaption, vision memory, etc.⁶). Mimicking the human retinal system has been inspiration for not only hardware R&D but also for development of signal & image processing algorithms that can result in future improvement in domains such as machine vision⁷, artificial intelligence⁸, and the Internet of Things⁹. The retina system consists of multiple cellular layers, where the outermost layer is the optical nerve cells that connects to the visual cortex to the brain, the intermediate layer consists of sub-layer networks responsible for neural signal transduction, and the bottom layer is responsible for light-to-neuronal signal conversion¹⁰. In human panchromatic vision, cone cells with signature monochromatic sensitivity of red (R), green (G), and blue (B) light at the bottom layer firstly sense the light and convert it to neuronal signals. And the intermediate layers further execute the pre-signal processing within its plexiform structure and transduce the signal to the outermost layer for further transmit to brain¹¹. Specifically, the R/G/B cone cells are able to individually convert photons of different wavelengths into neuronal signals, with a narrow optical band feature. And the intermediate cellular layer can execute both feed-forward and feedback control to simplify the signal being transmitted to the brain¹¹. Overall, the R/G/B cone cells are the basic units responsible for monochromatic photon detection of different wavelength and the network layer provides processing of the resultant neuronal signals that eventually transport to the brain to perceive the object.

Electronically sensing the object with a similar perception as that of the human eye can be achieved by photodetectors (PDs) that individually respond to the same range of wavelengths in the electromagnetic spectrum where human retina is responsive. Charge-coupled device (CCD) and complementary metal-oxide-semiconductor (CMOS) cameras have shown significant progress by using Si or InGaAs-based broadband sensor arrays^{12, 13}. Unlike the R/G/B retinal cone cells, these broadband sensor arrays^{12, 13} cannot *intrinsically* distinguish the color and usually need an external color filter array (CFA) to achieve monochromatic sensing. The insertion of CFA not

only increases the cost and manufacturing complexity but also causes spatial information loss due to the coplanar R/G/B dispersion by CFA as well as other issues such as color aliasing or color moiré effect¹⁴, and limited quantum efficiency¹⁵ (I/N) by channel numbers (N) in the CFA layout¹⁶. In these systems, a demosaicing process (digital calculation to process the ‘missing’ color values for each pixel in the raw capture)¹⁷ is typically needed to reconstruct a full-color image from the incomplete color samples output from an image sensor overlaid with a CFA. This additional computational complexity requires higher memory capacity and reduces the overall speed of the camera. In contrast, filter-free narrowband (NB) PDs could circumvent such issues by CFA exemption and optimized spatial arrangement. In analogous to the R/G/B cone cells in the human retina, NB PDs have the *intrinsic* monochromatic sensing capability. This capability can be achieved through mechanisms such as all-dielectric metasurface¹⁸, narrow absorption¹⁹, manipulation of Frenkel exciton dissociation²⁰, charge collection²¹, and surface-trap recombination²² across different materials including organics, two-dimensional inorganics, and halide perovskites. The halide perovskites bearing exceptional semiconducting properties such as long charge carrier diffusion length, high light extinction coefficient, and benign electronic band structure with high trap-tolerance²³ could be excellent NB PD candidate. Through compositional engineering, the NB response band can be tuned to R/G/B regions enabling the realization of individual pixel devices analogous to retinal cone cells.

Here, we demonstrate an R/G/B NB PD array using engineered halide perovskite films fabricated from a volatile solvent (VS) system, followed by for a multi-layer algorithm to mimic human retina system for panchromatic imaging. Briefly, we observed that the perovskites obtained from this VS method exhibit heavily unbalanced electron-hole transfer property that electrons and holes could drift distinct distance towards corresponding electrodes. By sandwiching this unbalanced perovskite into different polar structures (p-i-n or n-i-p), photocurrent collection at electrode can be manipulated upon the wavelength-dependent photogeneration center along the thickness direction, which is due to the effect of wavelength-dependent optical field distribution (WDOFD). This unbalanced transport and WDOFD jointly enable the NB response of the PDs for individual R/G/B distinction. By using a vertical stacking of the six-terminal R/G/B layout, a full-color detection with the exemption of CFA (or demosaicing) has been achieved. Next, in order to mimic the intermediate network of the retinal system, we pass the raw current signal to a three-sub-layer neuromorphic algorithm for feed-forward signal processing. As a result, we demonstrate

the photo-electrical capturing and restoration of a 1024-pixel full-color image by a 32×32 perovskite NB PD sensor array with three R/G/B channels. The signals were further processed using a neuromorphic network algorithm to mimic the plexiform structure in the intermediate cellular layer in retina. The results of the perovskite array display a high-fidelity for panchromatic imaging. This system-level demonstration of the retina imaging process provides new insight for implementing panchromatic imaging techniques.

Results and discussion

Three types of natural R/G/B cone cells have been mimicked in imaging technology with three channels of R/G/B to realize panchromatic imaging. There can be two types of device architecture for panchromatic imaging. **Fig. 1a** compares the typical parallel²⁴ and stacking²⁵ design. The parallel architecture has been ubiquitously applied in the commercial digital camera, with the incident white light being spatially dispersed into R/G/B through a complimentary CFA followed by detection of a color-blind sensor array. Hence, a post logic processing to compromise issues of spatial resolution limit, optical efficiency, and color moiré is needed and this is provided by a complex back digital circuit (**Fig. 1a(i)**). In contrast, the stacking design allows the white light to penetrate into different photoactive layers to obtain separate monochromatic sensing without spatial dissipation (**Fig. 1a(ii)**), which can circumvent the abovementioned issues in those parallel designs. Coincidentally, it should be noted that similar vertical stacking strategies have also been applied in tandem solar cells to overcome the thermodynamic losses²⁶ and in a light emitting diode (LED) to have a full-color-tunability²⁷. The stacking structure is expected to deliver a higher light usage ratio on the unit area but also provide separate electrical channels for panchromatic color reconfiguration using a multi-layer algorithm analogous to that occurring in the retinal system. **Fig. 1b(i)** specifies the neurotransmitter network at the bottom side of the human eye (**Fig. 1b(ii)**). Briefly, the light-to-neuronal signal conversion first takes place at the R/G/B cone cells from the photoreceptor layer, and the network layer consisting of three-sub-layers of horizontal cells, bipolar cells, and amacrine cells to process the signal, followed by the transduction via the ganglion cell to deliver the signal to the brain. In analogy to this natural scheme, we designed a three-sub-layer neuromorphic algorithm to process the current signals from the R/G/B PDs (**Fig. 1c(i)**). In doing so, we developed the NB perovskite PDs arrays to mimic the cone cells (**Fig. 1d**) and transduce their electrical information towards the abovementioned neuromorphic algorithm. A

proof-of-concept result of three independent R/G/B channels in mimicking the retina layer of a primitive 15×8-pixel NB PD array is presented in **Fig. S1 (Supplementary Note 1)**.

The NB PDs are made from thin perovskite films ($\leq 2 \mu\text{m}$) of different halogen compositions (MAPbX_3 , $X = \text{Cl, Br, I}$ or their combination) for bandgap modulation. In order to obtain highly homogeneous crystalline film for retinal cellular arrays, we utilized the volatile solution (VS) method containing methylamine-liquified perovskites in volatile acetonitrile that enables the realization of ultra-uniform films (detailed in **Supplementary Note 2**). Through compositional engineering, MAPbX_3 with different halogen compositions were found to display varying absorption edges (**Fig. 2a**) spanning over the whole visible region from 452 nm to 700 nm (corresponding to 1.77 eV to 2.74 eV as plotted in **Fig. S5**). Since the p orbital of halogen in MAPbX_3 contributes to the valence band maximum (VBM), tuning the halogen could thereby modulate the bandgap accordingly. We developed the compositions $\text{MAPb}(\text{BrI}_2)$, $\text{MAPb}(\text{Br}_3)$, and $\text{MAPb}(\text{Cl}_{1.5}\text{Br}_{1.5})$ with absorption edge of 700, 549, and 470 nm, respectively, as the photoactive layer for the R/G/B NB detection. All the samples exhibit a narrow FWHM (full width half maximum) less than 55 nm from the photoluminescence (PL) spectra (**Fig. 2b**). It should be noted that the mixed halide perovskite synthesized using traditional nonvolatile methods, usually has serious phase separation issues owing to the halide ion migration^{28, 29} in the loosely crystallized materials. The phase separation will lead to bandgap splitting interfering the detection range of PD and the defect in poor crystals will cause performance output uniformity issue in the array application. In contrast, the film casted from the volatile solution (VS) displays compact and highly crystallized features without any phase separation for all the R/G/B samples. Taking the $\text{MAPb}(\text{BrI}_2)$ as an example, the X-ray diffraction (XRD) spectra shows strong (100) orientation with a high Lotgering factor (LF) of 0.92 (**Fig. 2c**), which is nearly three-time-higher than the reference $\text{MAPb}(\text{BrI}_2)$ film casted from traditional nonvolatile solution (LF of 0.31, **Fig. S6a**). Similarly, the $\text{MAPb}(\text{BrI}_2)$ film also displays a mono (100) peak at 14.46° , without characteristic peaks from any of the hypothetical separated I-rich or Br-rich phases (**Fig. S7**). To verify the mono-phase of the mixed halide R/G/B films, we also use the scanning transmission electron microscopy (STEM) coupled with a high angle annular dark-field (HAADF) detector to visualize the atomic distribution in these films. **Fig. 2d** shows the energy dispersive spectroscopy (EDS) mapping of Cl, Br, I, and Pb in different samples. The binary mixed halogen elements in either red- $\text{MAPb}(\text{BrI}_2)$ or blue- $\text{MAPb}(\text{Cl}_{1.5}\text{Br}_{1.5})$ films exhibit homogeneous halogen distribution over the

grain and there are no Br, I or Cl-rich phases separated within the grain. The single-halogen green-MAPb(Br₃) also shows the identical distribution of Pb and Br in the whole grain, indicating no noticeable impurities or segregation of Pb or Br. These results verify the crystalline phase purity of the perovskite films processed from our VS method, which is important for fabricating array PD device that needs high-standard uniformity and purity to deliver low signal-to-noise ratio. In addition, high reproducibility in array pixel devices also require high morphological homogeneity of the perovskite crystalline film. We also identify the film homogeneity of R/G/B perovskites processed from the VS method. **Fig. 2e** displays the top-view and cross-sectional scanning electron microscope (SEM) images of R/G/B perovskite films coated on PEDOT:PSS (poly(3,4-ethylenedioxythiophene) polystyrene sulfonate) hole transfer layer (HTL) substrate. All the R/G/B films display homogeneous and dense features, which will secure each integrated pixel device to have identical PD performance.

We then use these VS processed R/G/B films for making NB PD single-pixel devices, followed by laser-scribing-based manufacturing to integrate them into array architecture. In principle, in order to realize NB photodetection, the device needs to be featured by a narrow internal quantum efficiency (IQE) with a peak around the target wavelength window³⁰. In analogy to R/G/B retina cells, NB PD devices need to have a mono-peak IQE response at 700, 550, and 470 nm, respectively, to avoid the usage of external optical filter. Typical semiconductors with a fixed bandgap tend to absorb shorter wavelength light with energy larger than the bandgap. As schematically shown in **Fig. S10a**, both long-wavelength and short-wavelength photons can be absorbed and contribute to the photocurrent. This makes it difficult to distinguish the photocurrent from different wavelengths and hard to realize an intrinsic NB PD. In fact, to selectively collect photocarriers generated from long-wavelength light, the photocarriers generated by short-wavelength light need to be internally consumed (*i.e.*, reducing IQE to zero) while IQE of long-wavelength light needs to be maintained at a high level. There have been prior studies to realize IQE narrowing in both organic and perovskite PDs^{21, 22, 30, 31, 32, 33}. Particularly in perovskite PDs, experiments either rely on thick perovskite films (20-25 μm)^{32, 33} or single crystals (ultrathick to ca. 300 μm)²² to quench short-wavelength photocarriers³⁰ by intrinsic or extrinsic recombination centers^{21, 31}. Nevertheless, the requirement of ultrathick film and uncontrollable doping is hard to balance with the film homogeneity that is necessary for array device application. In contrast, here we develop the thin film (< 2 μm) perovskites for array structures of NB PDs, by implementing a

strategy of unbalanced electron-hole transport. This thin film is highly controllable in uniformity and reaches the application benchmark desired for multi-pixel array retinal chip.

In principle, along the perovskite thickness direction, there is a wavelength-dependent optical field distribution (WDOFD) of the incident light due to the wavelength-dependent variation of optical constants (i.e., refractive index $n(\lambda)$ and extinction coefficient $k(\lambda)$)³⁴. Taking the red-MAPb(BrI₂) NB PD (with a p-i-n structure of ITO/PEDOT:PSS/MAPb(BrI₂)/PCBM/Au) as an example, **Fig. 3a** shows the simulated optical field distribution of incident light of different wavelengths along the thickness direction. Short-wavelength light (e.g., from 350 to 550 nm) can be quickly absorbed near the surface region and beyond 1 μm there is negligible photocarrier generation from the short-wavelength. The long-wavelength light (e.g., 650 nm) penetrates deeper through the perovskite film and generates the photocarriers over the whole thickness region (**Fig. S11a**). Similarly, both green-MAPb(Br₃) and blue-MAPb(Cl_{1.5}Br_{1.5}) perovskite films also display this WDOFD effect (**Figs. S12a & S13a**). As exemplified in **Fig. S14a**, in a p-i-n device configuration, short-wavelength generated electrons (generated at front side) need to drift a long distance (through the film thickness) to reach the backside cathode. This makes it possible to minimize the collection efficiency of these short-wavelength generated electrons by using a perovskite with low electron mobility. In parallel, due to the deeper penetration of long-wavelength light, long-wavelength photoelectrons generated close to the cathode side can be collected due to a shorter drift distance (**Fig. S14b**). In order to ensure a good hole collection from these deeper generation sites, good hole mobility is required for the perovskite.

We demonstrate that the NB PD can be achieved using the perovskite with an unbalanced electron-hole mobility ($\mu_h > \mu_e$) in a p-i-n configuration (details are demonstrated in **Supplementary Note 3**). It should be noted that the perovskite film fabricated from using our volatile solvent (VS) method exhibits this desired unbalanced photocarrier transport property. We verified this by characterizing the charge transport properties using monotype carrier-type diodes coupled with both electrical and photoluminescence (PL) investigations (detailed description, calculation, and discussion are specified in **Supplementary Note 4**). Briefly, **Fig. 3b** shows the J-V characteristics of red-MAPb(BrI₂)-based electron-only and hole-only diodes in the dark as an example, from which key transport parameters such as carrier mobility can be extracted using the space-charge-limited current (SCLC) method³⁵. As a result, the red-MAPb(BrI₂) displayed a μ_h of $2.61 \times 10^{-4} \text{ cm}^2 \text{ V}^{-1} \text{ s}^{-1}$, which is 6-fold higher than its μ_e of $4.19 \times 10^{-5} \text{ cm}^2 \text{ V}^{-1} \text{ s}^{-1}$. To further

confirm the presence of this unbalanced electron-hole transport in a photophysical process, we performed the time-resolved PL (TRPL) spectroscopic studies on the MAPb(BrI₂)-based electron-only (TiO₂/Perovskite/PCBM) and hole-only (PEDOT: PSS/Perovskite/Spiro-OMeTAD) samples (**Fig. 3c**). The hole-only sample exhibits a much faster average decay lifetime $\tau_{ave,h}$ of 2.36 ns than that of electron-only sample ($\tau_{ave,e}$ of 18.09s), which is consistent with the result of their time-integrated PL (**Fig. S16a**). In comparison, we also measured samples with a similar structure using perovskite prepared from the conventional nonvolatile solvent of dimethylformamide and dimethyl sulfoxide. As shown in **Fig. S16d**, conventional MAPb(BrI₂) displays the $\tau_{ave,h}$ and $\tau_{ave,e}$ at similar level *ca.* 10 ns which is consistent with its balanced electron-hole mobility nature. The VS prepared red-MAPb(BrI₂) displays an over 7-fold smaller $\tau_{ave,h}$ indicating a much more efficient photogenerated hole transfer and extraction/bleaching from the red-MAPb(BrI₂) to the quencher. This is consistent with its higher μ_h that a faster hole transfer towards the quencher quickly reduces their lifetime in the film. Hence, the VS prepared red-MAPb(BrI₂) displays a more efficient hole transfer than the electron. We also characterized the mobility and average lifetime for VS prepared green-MAPb(Br₃) and blue-MAPb(Cl_{1.5}Br_{1.5}) perovskites and observed the similar unbalanced transport behavior (detailed quantitative discussion on mechanisms are included in **Supplementary Note 4**).

We then utilized these VS-prepared perovskites coupled with the WDOFD effect to devise the R/G/B NB PDs. By using an asymmetric p-i-n configuration of FTO/PEDOT:PSS/RGB perovskite/PCBM/Au, we observed mono-peak EQE in R/G/B under zero bias (**Fig. S19**). This power-free detection feature is due to the work function difference of cathode and anode materials that form an intrinsic electric field to drive the photogenerated electrons and holes moving towards corresponding electrodes. As a result, under zero bias, we successfully obtained NB responses of 640-720, 530-570, and 460-500 nm lying in the red, green, and blue color regimes, respectively. **Fig. S20** displays the responsivity (R) of R/G/B NB PDs calculated from the equation:

$$R = EQE \frac{e}{h\nu} (A W^{-1}) \quad (1)$$

where e is the elementary charge, h is the Planck's constant, and ν is the frequency of light, respectively. The R/G/B NB PDs display a responsivity peak of 4, 3.5, and 2 mA W⁻¹ at zero-bias, respectively, which approaches the state-of-art perovskite NB PDs (e.g., 10 mA W⁻¹) but under large bias as 4 V^{22, 32, 33}. This result provides the proof-of-concept of the NB response realized by our thin film perovskites with unbalanced transport coupled with the WDOFD effect.

Next, in order to understand the correlation of PDs with the R/G/B retinal cells, we characterize the devices in terms of spectral detectivity, temporal response, and optical linearity. Here we use the red PD as an example for simplification and include the related demonstrations on green and blue PDs in **Supplementary Note 5**. **Fig. 3d** shows the J–V plot of the red PD under 650 nm irradiation and dark condition, respectively. It should be noted that under zero bias the PD displays a low dark current density of *ca.* 10^{-7} A cm⁻² but a high light current of 5×10^{-3} A cm⁻², and thus a high on/off ratio (I_{on}/I_{off}) over 10^3 . The specific detectivity (D^*) of PD can be determined from equation³⁶:

$$D^* = \frac{\sqrt{A}}{NEP} (\text{Hz}^{-1/2} \text{ cm W}^{-1}) \quad (2)$$

where A is the working area of PD (here A is 0.1 cm²) and NEP is the noise equivalent power which can be calculated from equation³⁶:

$$NEP = \frac{R}{i_n} (\text{W Hz}^{-1/2}) \quad (3)$$

with R being responsivity and i_n being the noise current value. We obtained the i_n from the noise spectra density derived from the Fourier transform of the dark current density versus time at zero bias. As shown in **Fig. 3e**, the red PD displays a noise current of 20 fA Hz^{-1/2}. **Fig. 3f** displays the specific detectivity spectrum of the red PD under zero bias, with a peak value of 6×10^{10} Jones (Hz^{1/2} cm W⁻¹) which is comparable to that of PD from prior researches but operating at high bias voltage (e.g., 10^{11} jones under 5 V)^{22, 31}. The detectivity bleaching is also present outside the response window, securing the monochromatic light response.

We also characterize the temporal response of the PDs, since the response speed is crucial for practical applications such as image sensors and it sets the limit on the framerate of image capturing³⁷. **Fig. S21** shows the current temporal response of red PD operating at zero bias under periodic illumination from a red 650 nm LED (light emitting diode). **Fig. 3g** shows the corresponding response zoomed-in on one period, with quantified rise time (t_{rise} , time for photocurrent rises from 10% to 90% of the peak value) and drop time (t_{drop} , time for photocurrent decreases from 90% to 10% of the peak value). The red PD displays a fast t_{rise} of 1.25 ms and t_{drop} of 1.31 ms comparable to typical broadband perovskite-based PDs^{38, 39} and almost one-order magnitude faster than that of human eyes (ca. 10 ms)⁴⁰ for pattern recognition. To further evaluate the response speed, we measured the frequency-dependent current response in **Fig. 3h**. The response bandwidth (f_{-3dB}) quantifies the response speed, which is the characteristic light

switching frequency at which the PD photocurrent drops to 70.7 % of its maximum value at the steady illumination condition (0 Hz)³⁷. The red NB PD exhibits a f_{-3dB} of 17.8 kHz, which represents a fast response speed among all the reported perovskite or organic NB PDs^{22, 31, 33} (20 - 700 Hz). Lastly, we assess the response linearity of the NB PDs with respect to incident light. **Fig. 3i** shows photocurrent dependence on the incident power with the linear dynamic range (LDR) estimated from equation⁴¹:

$$LDR = 20 \times \log \frac{P_{max}}{P_{min}} \text{ (dB)} \quad (4)$$

where P_{max} and P_{min} are the boundary limits of the optical power within which the current has a linear relationship with the power. Overall, at room temperature, the red PD displays an LDR of 70.4 dB, which is higher than that of InGaAs-based PDs (66 dB, at 4.2 K) and approaching that of Si-based PDs but operating at ultralow temperatures (120 dB, at 77 K)⁴². We also characterize these figure-of-merits in both green and blue PDs, detailed in **Supplementary Note 5**. As expected, all the R/G/B PDs display a narrow response band (FWHM \leq 50 nm), quick response ($t_{rise}, t_{drop} \leq$ 1.6 ms, f_{-3dB} of 6-18 kHz), and good linearity ($LDR \geq$ 70 dB), indicating good qualification for the next array usage.

We then utilize these R/G/B NB PDs as pixel devices in an array structure manufactured by the pico-second laser-scribing technique (**Fig. S26, Supplementary Note 6**). For demonstration purpose, we made three chips of R/G/B containing 10×10-pixel devices with a pixel area of 1 mm² (detailed design and readout circuit are presented in **Fig. S27a**). **Fig. S28** displays the testing setup, where we used a projector (M6 Pico Projector, AAXA Technologies) to generate a panchromatic source image and utilized a lens to focus the incident light onto the chips. Blue, green, and red chips are sequentially stacked (6 terminal stacking) from front to back, where blue, green, and red channels of current are read out independently. These signals are further transferred to a neuromorphic network analogous to the bipolar, horizontal, and amacrine cells in the human retinal system (**Fig. 1b(i)**) to execute the image restoration. **Fig. 4a** displays the selective spectra response within the red, green, and blue regimes of our R/G/B PDs. It should be noted that the perovskite can be engineered to have a broad bandgap range, which enables panchromatic imaging using multiple color channels. Here we construct the R/G/B stacking chips as an example. Each R/G/B NB PD chip only detects the corresponding color without any interference with others. To demonstrate this, we tested the stacking chips with a color mixing pattern (**Fig. S29a**). **Figs. S29c-S29e** show the photocurrent mapping from red, green, and blue channels, respectively, where there

is a good color distinguishment between different lights and no obvious interfering noise signal from other colors. The results also show good color uniformity due to the high film uniformity, which is important for image capturing and reconstruction. To further quantify the color distinguishing ability, we also test the green chip with a color-blind pattern that is normally used for human color vision tests. As can be seen in **Fig. S31**, the chips could distinguish the clear “checkmark” pattern from the original image and there is two order-of-magnitude difference in current intensity between “checkmark” region and the background region. These results suggest good distinguishing in color mixing pattern in primitive 10×10 -pixel NB PD arrays. Notably, all these results are measured under zero bias conditions so that this light-driven detection without power supply is analogous to the natural retinal cells and it does not require battery that typical commercial camera needs.

In order to further confirm the down-scalability of pixel size with respect to signal noise ratio and NB PD performance, we constructed 32×32 -pixel chips for red, green, and blue PD arrays (pixel area of $33\times 33\ \mu\text{m}^2$, a photo of a red chip is presented in **Fig. 1d**). For testing, we use a 949-byte (32×32 -pixel, 96 dpi, 24-bit depth) color image (*sunflower* picture, **Fig. 4c**) as the source image for panchromatic imaging using our R/G/B chips. **Figs. 4b(i)-b(iii)** show the photocurrent mapping under zero bias in red, green, and blue channels obtained from corresponding chips. The photocurrent maps clearly show the R/G/B feature of the original image with sharp contrast and high fidelity. To reconstruct the original panchromatic *sunflower* image and compare the algorithm excellence between a typical merging reconstruction and a retinal system mimicked multilayer neuromorphic reconstruction, here we use two different reconstruction methods, i.e., (i) channel merging and (ii) machine learning. The channel merging method first normalizes 2D current values to pixel intensity values, with the lowest current shifting to 0, highest to 255, and other values scaling linearly. After further converting floating-point normalized values to integers, the *sunflower* image is directly reconstructed by stacking pixel intensity integers from R/G/B channels, as shown in **Fig. 4c(ii)**. It is worth mentioning that a minimum pixel value of 0 is observed for all three R/G/B channels from the original image (shown in **Fig. 4c(i)**), and the maximum pixel value of 255 is also observed for all channels. These observations guarantee that current values best correlate with pixel values, indicating the best channel merging reconstruction quality. On the other hand, machine learning reconstruction adopts a multilayer perceptron neural network that takes current values as input and predicts pixel values as output accordingly, which can be

analogous to the multilayer structures of horizontal, bipolar, and amacrine cells in the retinal system (**Fig. 1b**). The neural network model relies on a set of training data points which refer to 1024 pairs of current values (features) from NB PD chips and pixel values (labels) from full-color *sunflower* images. The i.i.d.⁴³ assumption of the training dataset is satisfied since each current value is independently measured using the same sensor array. A standard neural network architecture (A2) is shown in **Fig. 1c** where the input layer contains 3 neurons corresponding to current values from three channels, respectively. In the middle, three hidden layers with respective 32 (H1, in analogy to horizontal cell layer), 64 (H2, in analogy to bipolar cell layer), and 32 (H3, in analogy to amacrine cell layer) neurons perform the black-box-like mapping from input to output. A learning algorithm usually has another testing dataset for evaluating the possible overfitting problem. For data acquiring simplification and concept-proof demonstration, we use the single *sunflower* image (1024 separate data points) for training and testing the learning algorithm (A2). Another two neural network learning algorithms are created with architectures 16-32-16 (A1) and 64-128-64 (A3) for the middle three hidden layers so as to demonstrate the better model complexity of A2. The learning algorithms are trained with batch sizes of 1 using Adam optimizer with default beta1 0.9 and beta2 on a single RTX 2080 Ti GPU. The learning rate is initially set to 0.001 for the first 100 training epochs and decays to 0.0005 for the second 100 epochs. Smooth L1 loss is adopted to reflect the learning quality. Furthermore, peak signal-to-noise ratio (PSNR), which shows the ratio between the maximum possible power of a signal (original *sunflower* image) and the power of the same image with noise (reconstructed image), is also calculated along with each training epoch for indicating learning quality.

As shown in **Fig. 4d**, a lower loss and a higher PSNR are observed in general for the standard model A2, suggesting the lighter model A1 is underfitting. Similarly, **Fig. 4e** displays the learning result comparison between A2 and A3, and the generally same level of loss and PSNR are observed, indicating the heavier model A3 is overfitting. It should be noted that the sharp curve change at epoch 100 is caused by the learning rate switching to a lower one. After 200 epochs, predicted pixel values from the standard model are converted to unsigned integers of 8 bits and then used to reconstruct the *sunflower* image (shown in **Fig. 4c(iii)**). It is worth mentioning that predicted pixel values have some values above 255 for the R channel in the upper left and right corners, and some values below 0 for the B channel in the middle. After converting to integers, these overflow and underflow values incur significant discrepancies (e.g., 260 converted to 4, -5

converted to 251), shown with strikingly different patches. Thus, a filtering scheme that sets all overflow values to 255, and underflow values to 0 is adopted before conversion into integers. The reconstruction result after taking the filtering scheme is shown in **Fig. 4c(iv)**. PSNRs before (25.49) and after (25.52) the filtering scheme do not have much difference since the number of pixel values having significant discrepancies is small. The PSNRs is much larger than the one from the channel merging reconstructed image since sensor array configuration error and measurement noise are inherently adjusted and mitigated within the machine learning algorithms. As a result, the reconstructed result in **Fig. 4c(iv)** shows nearly no difference compared with the original image in **Fig. 4c(i)**. The advantage of the machine learning algorithm over the typical channel merging method is further discussed in **Supplementary Note 7**. These results demonstrate a promising retina-inspired imaging sensor that combines the R/G/B perovskite NB sensor array (mimicking the R/G/B cone cells) with the neuromorphic algorithm (mimicking the intermediate network of the retinal system), which is capable of high-quality panchromatic imaging.

Conclusion

In summary, we demonstrate several fundamental breakthroughs in this study in realizing perovskite NB PD chips for panchromatic imaging, from material synthesis to device design to system innovation. Briefly, we successfully obtain the highly uniform R/G/B perovskite thin films ($< 2 \mu\text{m}$) with heavily unbalanced electron-hole mobility ($\mu_h/\mu_e \sim 5$) based on a volatile solvent method. By inserting these films into a p-i-n architecture, the unbalanced electron-hole transport and the WDOFD effect synergistically leads to an NB detection with excellent performance in bandwidth, response speed, and optical linearity. Taking advantage of the good film uniformity, we devise R/G/B image sensing chips using laser-scribing techniques and collect R/G/B photocurrent signals independently. Inspired by the retinal system, we combine the R/G/B perovskite NB chips (mimicking the R/G/B cone cells) with a tri-layer algorithm (mimicking the intermediate network of the retinal system) and successfully realized panchromatic imaging. It is also worth noting that our perovskite NB PDs constructed in the asymmetric p-i-n configuration can have NB detection under zero external bias. This light-driven panchromatic imaging may trigger further development in applications such as battery-free cameras, light-driven sensing, artificial retina replaceable for dead retina cells in vision damages, etc.

Acknowledgment

Y.H., K.W. and S.P. acknowledge the financial support from the Air Force Office of Scientific Research (AFOSR award number FA9550-20-1-0157). J. Y. acknowledges the support from the U.S. Department of Energy Award No. DE-SC0019844, under the STTR program (Prime – NanoSonic Inc.). D.Y. acknowledges the support from National Science Foundation (NSF award number 1936432). A.M.K. acknowledges the support from the National Institute of Food and Agriculture (NIFA award number 2019-67021-28991). L. Z. acknowledges the support through Huck Institute of the Life Sciences seed grant (HITS). K.W. especially thanks graphic engineer Jingyu Fang's help in discussion of conceptualization of this work.

Disclaimer:

"This report was prepared as an account of work sponsored by an agency of the United States Government. Neither the United States Government nor any agency thereof, nor any of their employees, makes any warranty, express or implied, or assumes any legal liability or responsibility for the accuracy, completeness, or usefulness of any information, apparatus, product, or process disclosed, or represents that its use would not infringe privately owned rights. Reference herein to any specific commercial product, process, or service by trade name, trademark, manufacturer, or otherwise does not necessarily constitute or imply its endorsement, recommendation, or favoring by the United States Government or any agency thereof. The views and opinions of authors expressed herein do not necessarily state or reflect those of the United States Government or any agency thereof."

Author contribution

S.P. designed the concept of artificial retina using organic-inorganic materials combined with biomolecules. S.P. and K.W. supervised and administrated the project. K.W. and Y.H. developed the material compositions and processing for pixel arrays. Y.H. and D.Y. performed the material synthesis and characterization analysis, Y.H. and J.Y. designed and fabricated the photodetector arrays, Y.H., L.Z. and T.Y. performed the photodetector performance evaluation and imaging test. J.L. and S.G. developed the neuromorphic algorithm for signal processing and image reconstruction. K.W. and Y.H. prepared the first draft of manuscript. All the authors have discussed the research data, reviewed the manuscript, and provided comments.

Figures and captions

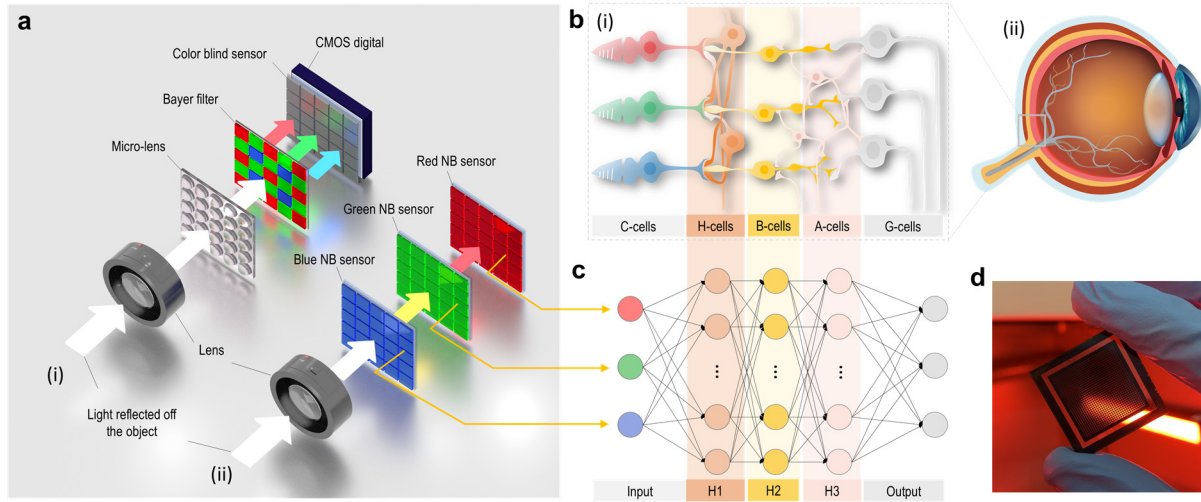


Figure 1 Overall design of retina-inspired narrowband perovskite photodetector for panchromatic imaging. (a) Schematic illustration of (i) typical parallel and (ii) stacking designs of panchromatic imaging sensor. (b) (i) Schematic of the multi-layer neurotransmitter network at the bottom of the retina in (ii) the human eye. (c) Schematic showing the three-layer neuromorphic algorithm for signal processing and image reconstruction. (d) A photo of a perovskite narrowband photodetector array made in this work. Note: C-, H-, B-, A-, G-cells are short for cone, horizontal, bipolar, amacrine, and ganglion cells, respectively. H1, H2, and H3 are the three hidden layers in the neuromorphic algorithm.

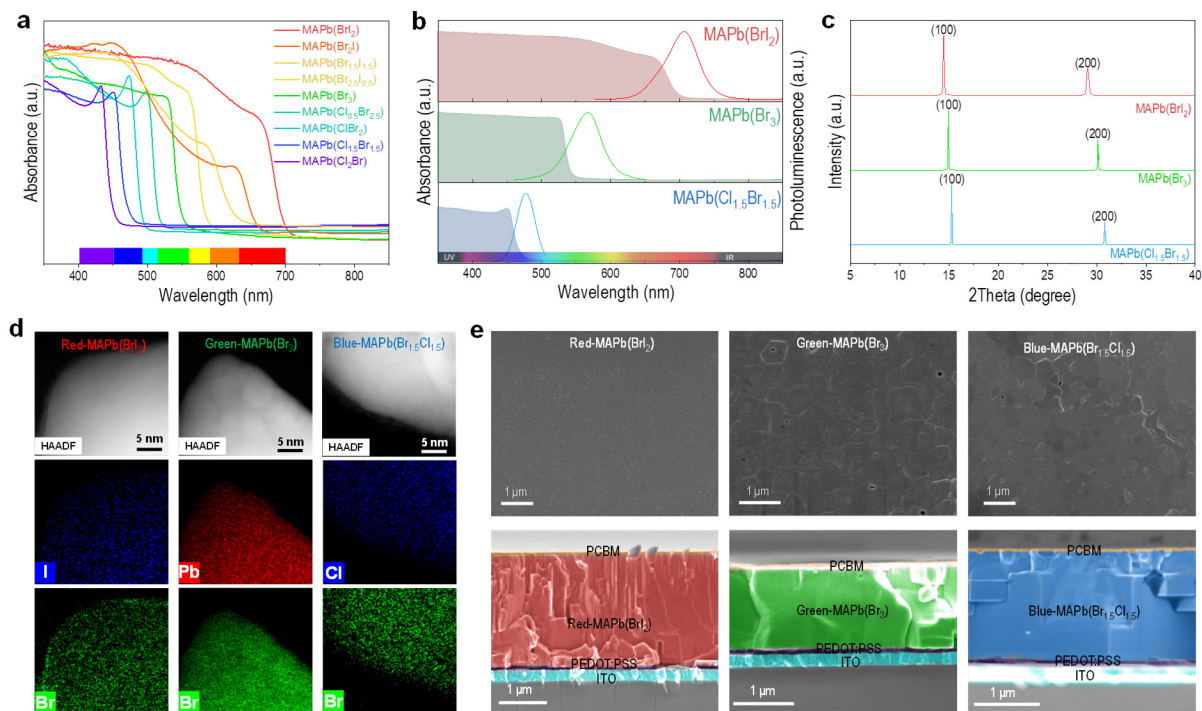


Figure 2 Materials characterization. (a) UV-Vis absorption spectra of perovskite film with different compositions. (b)-(e): (b) UV-Vis absorption and photoluminescence (PL) spectra, (c) X-ray diffraction (XRD) pattern of perovskite thin films, (d) elemental mapping of perovskite crystals, (e) top-view SEM images of perovskite thin film (upper row) and cross-sectional SEM images (lower row) showing the layout of red-MAPb(Br₂), green-MAPb(Br₃) and blue-MAPb(Cl_{1.5}Br_{1.5}) photodetector.

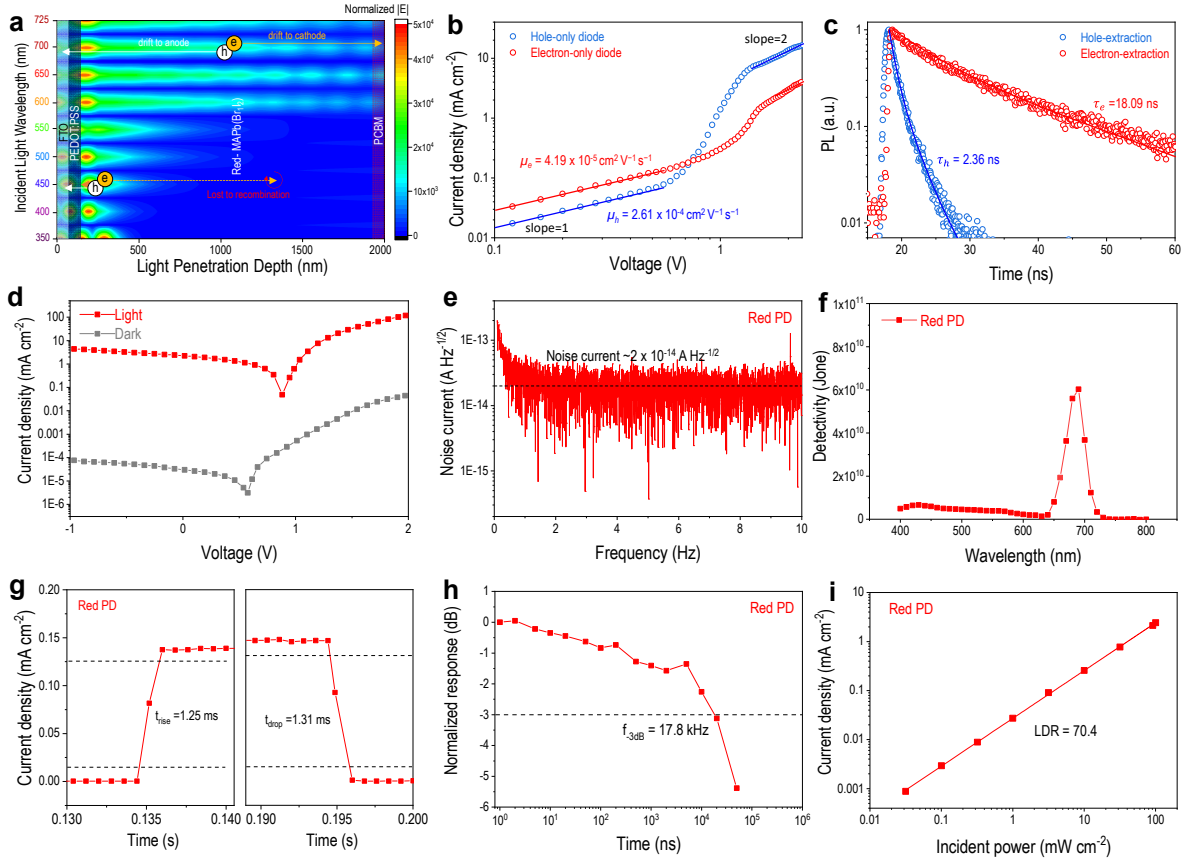


Figure 3 Working mechanism and performance of red-MAPb(BrI₂) narrowband-photodetector (NB PD). (a) Wavelength-dependent optical field distribution (WDOFD) of the incident light due to the wavelength-dependent variation of optical constants of the perovskite. (b) Current density–voltage (J – V) characteristic of the electron-only diode and hole-only diode of red-MAPb(BrI₂) measured in dark. (c) Time-resolved photoluminescence (TRPL) of electron- and hole-extraction structure of red-MAPb(BrI₂). (d) J – V curve of red NB PD measured in the dark and under 650 nm LED light illumination. (e) Noise current of red NB PD. (f) Specific detectivity (D^*) of red NB PD at zero-bias condition, measured from full wavelength spectrum. (g) Zoom-view of J – t curve showing a single light on/off state of red NB PD. (h) Frequency-dependent output response of red NB PD. The dashed line shows the representative -3 dB bandwidth (f_{-3dB}) of 17.8 kHz. (i) Current density with illumination power curve showing the linearity of red NB PD.

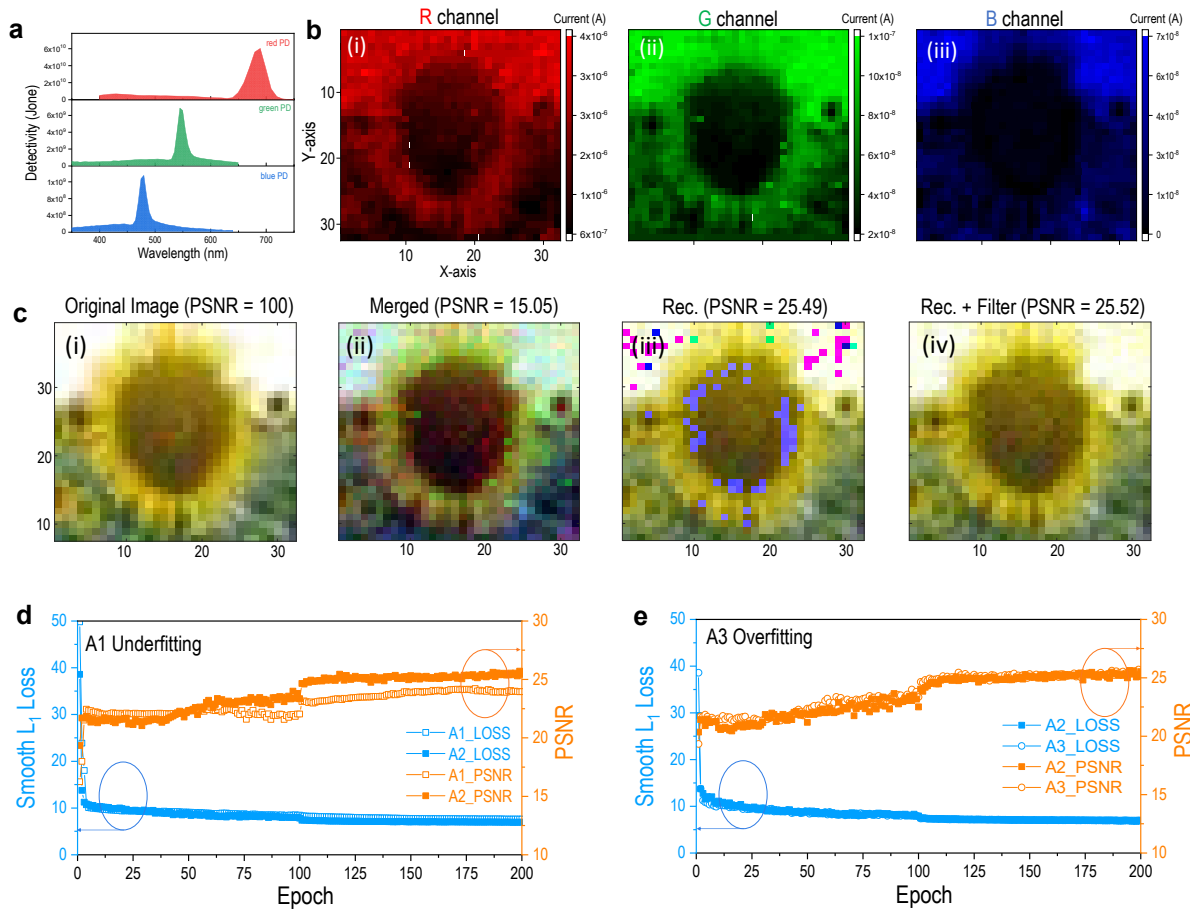


Figure 4 Panchromatic imaging test. (a) Detectivity spectra of red, green, and blue NB PDs showing their respective detection window. (b) 2D current mapping in (i) red (ii) green (iii) blue channels obtained from red, green, blue NB PD arrays with $32 \times 32 = 1024$ pixels for each. (c) (i) Original image (ii)-(iv) restored images by different reconstruction methods: (ii) Direct channel merging (iii) Neuromorphic processing without filtering scheme (iv) Neuromorphic processing with filtering scheme. (d) Plot of smooth loss and peak signal-to-noise ratio (PSNR) with epoch for the standard model A2 (with 32-64-32 nodes in three hidden layers) and lighter model A1 (with 16-32-16 nodes in three hidden layers), showing that A1 is underfitting. (e) Plot of smooth loss and peak signal-to-noise ratio (PSNR) with epoch for the standard model A2 and heavier model A3 (with 64-128-64 nodes in three hidden layers), showing that A3 is overfitting.

Reference

1. Wei Y, Zhao Z, Song J. Urban building extraction from high-resolution satellite panchromatic image using clustering and edge detection. *IEEE International Geoscience and Remote Sensing Symposium (IGARSS) 2004*, p.2008-2010.
2. Jansen-van Vuuren R D, Armin A, Pandey A K, Burn P L, Meredith P. Organic photodiodes: the future of full color detection and image sensing. *Advanced Materials* 2016, **28**(24): 4766-4802.
3. Jacobs S. The History and Aesthetics of the Classical Film Still. *History of Photography* 2010, **34**(4): 373-386.
4. Tinsley J N, Molodtsov M I, Prevedel R, Wartmann D, Espigulé-Pons J, Lauwers M, *et al.* Direct detection of a single photon by humans. *Nature Communications* 2016, **7**(1): 12172.
5. Clark R. Notes on the Resolution and Other Details of the Human Eye. 2005.
6. Beck J, Hope B, Rosenfeld A. *Human and machine vision*, vol. 8. Academic Press, 2014.
7. Berco D, Shenp Ang D. Recent progress in synaptic devices paving the way toward an artificial cogni-retina for bionic and machine vision. *Advanced Intelligent Systems* 2019, **1**(1): 1900003.
8. Shi X, Chen H, Zhao X. REBOR: A new sketch-based 3d object retrieval framework using retina inspired features. *Multimedia Tools and Applications* 2021: 1-15.
9. Shi W, Guo Y, Liu Y. When flexible organic field-effect transistors meet biomimetics: a prospective view of the internet of things. *Advanced Materials* 2020, **32**(15): 1901493.
10. Steffen L, Reichard D, Weinland J, Kaiser J, Roennau A, Dillmann R. Neuromorphic stereo vision: A survey of bio-inspired sensors and algorithms. *Frontiers in neurorobotics* 2019, **13**: 28.
11. Reinhard E, Khan E A, Akyuz A O, Johnson G. *Color imaging: fundamentals and applications*. CRC Press, 2008.
12. Ko H C, Stoykovich M P, Song J, Malyarchuk V, Choi W M, Yu C J, *et al.* A hemispherical electronic eye camera based on compressible silicon optoelectronics. *Nature* 2008, **454**(7205): 748-753.
13. Chen S, Lou Z, Chen D, Shen G. An Artificial Flexible Visual Memory System Based on an UV-Motivated Memristor. *Advanced Materials* 2018, **30**(7): 1705400.
14. Saveljev V, Kim S K, Kim J. Moiré effect in displays: a tutorial. *Optical Engineering* 2018, **57**(3): 030803.
15. Palanchoke U, Boutami S, Gidon S. Spectral sorting of visible light using dielectric gratings. *Optics Express* 2017, **25**(26): 33389-33399.
16. Gunturk B K, Glotzbach J, Altunbasak Y, Schafer R W, Mersereau R M. Demosaicking: color filter array interpolation. *IEEE Signal processing magazine* 2005, **22**(1): 44-54.

17. Walia G K. Image Demosaicing: A Roadmap to Peculiarity Imaging. *Turkish Journal of Computer and Mathematics Education (TURCOMAT)* 2021, **12**(11): 3614-3623.
18. Yang C, Wang Z, Yuan H, Li K, Zheng X, Mu W, *et al.* All-dielectric metasurface for highly tunable, narrowband notch filtering. *IEEE Photonics Journal* 2019, **11**(4): 1-6.
19. Siegmund B, Mischok A, Benduhn J, Zeika O, Ullbrich S, Nehm F, *et al.* Organic narrowband near-infrared photodetectors based on intermolecular charge-transfer absorption. *Nature communications* 2017, **8**(1): 1-6.
20. Xie B, Xie R, Zhang K, Yin Q, Hu Z, Yu G, *et al.* Self-filtering narrowband high performance organic photodetectors enabled by manipulating localized Frenkel exciton dissociation. *Nature communications* 2020, **11**(1): 1-9.
21. Lin Q, Armin A, Burn PL, Meredith P. Filterless narrowband visible photodetectors. *Nature Photonics* 2015, **9**(10): 687.
22. Fang Y, Dong Q, Shao Y, Yuan Y, Huang J. Highly narrowband perovskite single-crystal photodetectors enabled by surface-charge recombination. *Nature Photonics* 2015, **9**(10): 679.
23. Wang K, Yang D, Wu C, Sanghadasa M, Priya S. Recent Progress in Fundamental Understanding of Halide Perovskite Semiconductors. *Progress in Materials Science* 2019: 100580.
24. Verhoeven G. Basics of photography for cultural heritage imaging. *3D recording, documentation and management of cultural heritage*. Whittles Publishing, 2016, pp 127-251.
25. Tang X, Ackerman MM, Chen M, Guyot-Sionnest P. Dual-band infrared imaging using stacked colloidal quantum dot photodiodes. *Nature Photonics* 2019, **13**(4): 277-282.
26. Yang D, Zhang X, Hou Y, Wang K, Ye T, Yoon J, *et al.* 28.3%-efficiency perovskite/silicon tandem solar cell by optimal transparent electrode for high efficient semitransparent top cell. *Nano Energy* 2021, **84**: 105934.
27. Zhang H, Su Q, Chen S. Quantum-dot and organic hybrid tandem light-emitting diodes with multifunctionality of full-color-tunability and white-light-emission. *Nature communications* 2020, **11**(1): 1-8.
28. Li W, Rothmann M U, Liu A, Wang Z, Zhang Y, Pascoe A R, *et al.* Phase segregation enhanced ion movement in efficient inorganic CsPbIBr₂ solar cells. *Advanced Energy Materials* 2017, **7**(20): 1700946.
29. Gualdrón-Reyes AsF, Yoon S J, Barea E M, Agouram S, Muñoz-Sanjosé V, Meléndez AnM, *et al.* Controlling the phase segregation in mixed halide perovskites through nanocrystal size. *ACS energy letters* 2018, **4**(1): 54-62.
30. Armin A, Jansen-van Vuuren R D, Kopidakis N, Burn P L, Meredith P. Narrowband light detection via internal quantum efficiency manipulation of organic photodiodes. *Nature communications* 2015, **6**(1): 1-8.

31. Li J, Wang J, Ma J, Shen H, Li L, Duan X, *et al.* Self-trapped state enabled filterless narrowband photodetections in 2D layered perovskite single crystals. *Nature communications* 2019, **10**(1): 1-10.
32. Wang J, Xiao S, Qian W, Zhang K, Yu J, Xu X, *et al.* Self-Driven Perovskite Narrowband Photodetectors with Tunable Spectral Responses. *Advanced Materials* 2021, **33**(3): 2005557.
33. Xue J, Zhu Z, Xu X, Gu Y, Wang S, Xu L, *et al.* Narrowband perovskite photodetector-based image array for potential application in artificial vision. *Nano letters* 2018, **18**(12): 7628-7634.
34. Genevet P, Capasso F. Holographic optical metasurfaces: a review of current progress. *Reports on Progress in Physics* 2015, **78**(2): 024401.
35. Murgatroyd P. Theory of space-charge-limited current enhanced by Frenkel effect. *Journal of Physics D: Applied Physics* 1970, **3**(2): 151.
36. Ahmadi M, Wu T, Hu B. A review on organic–inorganic halide perovskite photodetectors: device engineering and fundamental physics. *Advanced Materials* 2017, **29**(41): 1605242.
37. de Arquer F P G, Armin A, Meredith P, Sargent E H. Solution-processed semiconductors for next-generation photodetectors. *Nature Reviews Materials* 2017, **2**(3): 1-17.
38. Wang H, Kim D H. Perovskite-based photodetectors: materials and devices. *Chemical Society Reviews* 2017, **46**(17): 5204-5236.
39. Sun H, Tian W, Cao F, Xiong J, Li L. Ultrahigh-performance self-powered flexible double-twisted fibrous broadband perovskite photodetector. *Advanced Materials* 2018, **30**(21): 1706986.
40. Trafton A. In the blink of an eye. 2014.
41. Gong X, Tong M, Xia Y, Cai W, Moon J S, Cao Y, *et al.* High-detectivity polymer photodetectors with spectral response from 300 nm to 1450 nm. *Science* 2009, **325**(5948): 1665-1667.
42. Hegedus S S, Shafarman W N. Thin-film solar cells: device measurements and analysis. *Progress in Photovoltaics: Research and Applications* 2004, **12**(2-3): 155-176.
43. Clauset A. A brief primer on probability distributions. Santa Fe Institute; 2011.

Supplementary Files

This is a list of supplementary files associated with this preprint. Click to download.

- [retinaSIfinal.pdf](#)